scientific reports

Check for updates

OPEN

# Revealing neural resonance in neuronal ensembles through frequency response tests

Peng Zhang, Liuye Yao, Tianyi Yang, Yajun Lou, Wei Xu, Wei Jiang, Weitao Li, Xiaofei Ji✉, Fan Gao✉ & Zhiyu Qian✉

**Photobiomodulation emerges as a novel method to boost neuronal activities and brain function, with notable implications for treating brain disorders. Yet, the mechanisms and optimal frequency parameters of transcranial photobiomodulation are still unclear, which highlights a research gap in understanding how different stimulation frequencies affect neural responses. This study proposes a hypothesis that the nervous system exhibits resonance phenomena, suggesting that external stimuli near the system's resonant frequency trigger the strongest responses. We tested this by performing frequency response tests with pulsed transcranial near-infrared light (10–200 Hz) on mouse brains, monitoring neural responses across frequencies by analyzing cerebral blood flow, concentration of oxygenated hemoglobin, and neurophysiological activity in both cortical and deep brain regions. Our results reveal pronounced neural responses in cortical and deep brain areas at 60–80 Hz and 120–140 Hz, suggesting the potential existence of neural system resonance. Conceptually, the neural system appears to be modulatable by external stimuli, reaching maximal neural response when the stimulation frequency aligns with the system's resonant frequency, leading to neural resonance. These findings will expect to become guide new theoretical frameworks and strategies for neural modulation and therapeutic interventions.**

**Keywords** Neural resonance, Photobiomodulation, Near-infrared light, Neuromodulation

Transcranial photobiomodulation (PBM) therapy, also known as transcranial low-level laser therapy (LLLT), represents an innovative approach for treating neurological and psychological disorders through the application of low-level red and near-infrared light to modulate nervous system activity[1–3]. The discovery of photobiomodulation by Endre Mester in 1967, along with subsequent observations of accelerated wound healing[4] and hair regrowth[5] in rats, led to the widespread clinical application of PBM for various brain disorders, including traumatic brain injuries (TBI), neurodegenerative diseases, and psychiatric conditions. The underlying mechanism is believed to involve photochemical reactions that adhere to the Grotthuss-Draper law, requiring light absorption by specific chemical substances such as cytochrome c oxidase (CCO)[6] to initiate photochemical processes. As a pivotal respiratory enzyme within the mitochondrial electron transport chain, CCO serves as the primary light-absorbing chromophore, significantly influencing LLLT's therapeutic effects on brain function[4,7]. The interaction between light and CCO is considered fundamental to mediating PBM's therapeutic benefits, representing a substantial advancement in non-invasive neurological treatments.

Nevertheless, considerable variability exists in the light frequencies used to treat different disorders, and the neural mechanisms underlying optimal frequency selection remain poorly understood. For instance, 10 Hz pulsed light is commonly employed for conditions such as TBI[8–10], Alzheimer's disease[11,12], age-related cognitive impairment[13], and depressive-like behaviors[14,15]. In contrast, 100 Hz stimulation is preferred for addressing behavioral deficits[16] and chronic mild stress[17]. Additionally, 40 Hz pulsed light has been shown to significantly modulate alpha, beta, and gamma oscillation frequencies, providing preliminary evidence for transcranial PBM's ability to influence neural oscillations[18,19]. In clinical practice, the optimal stimulation frequency often varies among individuals, and methods for adaptively adjusting stimulation parameters according to individual differences have yet to be developed[12]. Given these considerations, the theoretical foundation for selecting specific frequencies in LLLT-mediated neuromodulation remains insufficient. The central challenge lies in

Department of Biomedical Engineering, Key Laboratory of Multi-modal Brain-Computer Precision Drive Ministry of Industry and Information Technology, Key Laboratory of Digital Medical Equipment and Technology of Jiangsu Province, Nanjing University of Aeronautics and Astronautics, Nanjing 210016, China. ✉email: jinxiaofei@nuaa.edu.cn; gfbme@nuaa.edu.cn; zhiyubme@163.com

understanding the nonlinear electrophysiological response characteristics of neural nuclei following optical stimulation at different frequencies.

In recent years, another phenomenon known as stochastic resonance has been identified in the context of brain electrophysiology. This phenomenon describes the enhanced responsiveness of nonlinear systems to weak periodic signals when accompanied by noise of appropriate intensity[20,21]. Stochastic resonance occurs widely across physical and biological systems and plays a crucial role in understanding information processing and environmental adaptation in living organisms. However, previous research has primarily focused on oscillatory characteristics within or between neural nuclei, or on resonance phenomena under random noise perturbations. Systematic investigations characterizing multilevel brain activity in response to external near-infrared (NIR) light stimulation at different frequencies remain scarce. To address this gap, we propose the concept of neural resonance, which refers to the frequency-specific enhancement of neural responses when the nervous system is stimulated at particular frequencies. This phenomenon arises from specific interactions between the nervous system and external stimuli, with only stimuli near the system's intrinsic frequency capable of producing significantly amplified neural responses. This mechanism may represent a fundamental aspect of near-infrared light-mediated neuromodulation.

To test this hypothesis, we designed frequency response experiments aimed at plotting stimulation frequency-neural response curves and identifying characteristic peaks indicative of neural resonance. We utilized pulsed transcranial near-infrared light (tNIR) at a wavelength of 810 nm and an intensity of 50 mW/cm, with pulse frequencies varying pseudo-randomly from 10 to 200 Hz to stimulate the mouse brain. Neural responses [2]were quantified using both optical imaging and electrophysiological techniques to measure four key parameters. To comprehensively capture hemodynamic and metabolic aspects of neural activity, we included measurements of cerebral blood flow (CBF) and oxygenated hemoglobin ($HbO_2$) concentration, which serve as established indirect indicators of neural activity through neurovascular coupling mechanisms. According to this principle, increased neuronal activity triggers enhanced blood flow to deliver oxygen and nutrients to active brain regions. While CBF changes reflect the hemodynamic response to metabolic demands, $HbO_2$ levels measured via optical imaging indicate oxygen delivery supporting neuronal metabolism during activation. These hemodynamic measures complement direct electrophysiological recordings—including electrocorticography (ECoG), spike firing rates (FR), and local field potentials (LFP)—by providing insights into the metabolic and vascular correlates of neural responses. Therefore, this study incorporated CBF and $HbO_2$ measurements to capture the multidimensional effects of pulsed tNIR stimulation, enabling a comprehensive evaluation of neural resonance across both hemodynamic and electrophysiological domains. Specifically, we quantified: (1) relative changes in cortical oxygenated hemoglobin concentration ($\Delta[HbO_2]$), (2) relative changes in cerebral blood flow ($\Delta$[CBF]), (3) sample entropy of ECoG, and (4) spectral power of ECoG in the mouse cortex[22–24]. Additionally, neural responses in deep brain regions (hippocampal CA1) were assessed using FR and LFP spectral power as quantitative indicators alongside cortical measurements. To further elucidate the underlying mechanisms, we employed computational modeling of small-world neural networks to validate the observed neural resonance phenomena, ensuring alignment with our experimental findings.

In summary, this study aimed to systematically characterize neural response patterns induced by near-infrared light stimulation, elucidate the effects of different stimulation frequencies on brain activity and neurodynamics, and determine whether resonance phenomena contribute to the mechanism of near-infrared light-mediated neural stimulation.

## Results

### Exploring neural resonance by investigating frequency responses of Δ[CBF] in cortex

To validate the existence of neural resonance phenomena in the brain, we initiated our study with a frequency response test of cerebral blood flow. Specifically, we stimulated the mouse cerebral cortex with a set of different pulsed tNIR frequencies while measuring $\Delta$[CBF] before and during stimulation using laser speckle contrast imaging (LSCI) technology[25–28]. This allowed us to assess the frequency response characteristics of tNIR-induced changes in $\Delta$[CBF] (Fig. 1a-b). Pseudo-colored images demonstrate the cerebral blood flow velocities under pulsed tNIR stimulation across a frequency range of 10–200 Hz (Fig. 1c). Our analysis revealed that $\Delta$[CBF] during tNIR stimulation (Dur-$\Delta$[CBF]), compared to the $\Delta$[CBF] prior to tNIR stimulation (Pre-$\Delta$[CBF]), significantly increased across all tNIR frequencies ranging from 10 to 200 Hz ($n = 10$ mice, $p < 0.0001$) (Fig. 1d). These findings indicate that tNIR pulses can enhance cortical $\Delta$[CBF] irrespective of tNIR frequency. However, it remains unclear whether the net change in stimulation-induced $\Delta$[CBF] varies with different tNIR stimulation frequencies. This raises the question of whether pulsed tNIR offers frequency-specific control over changes in $\Delta$[CBF]. To exploreit, we examined net change in $\Delta$[CBF] by subtracting Pre-$\Delta$[CBF] from Dur-$\Delta$[CBF], which represents the modulation in $\Delta$[CBF] resulting from the application of tNIR. Results showed a continuous upward trend in the average level of $\Delta$[CBF] within the 10–50 Hz stimulation range. A significant peak was observed in the 60–80 Hz tNIR frequency band ($n = 10$ mice, $p < 0.0001$ compared with 10–50 Hz, 90–110 Hz, and 150–200 Hz; NS compared with 120–140 Hz) (Fig. 1e). This was followed by a decline to the level of the 50 Hz tNIR frequency range starting at 90–110 Hz. A second significant peak emerged in the 120–140 Hz tNIR frequency range ($n = 10$ mice, $p < 0.01$ compared with 10–50 Hz, 90–110 Hz, and 150–200 Hz; NS compared with 60–80 Hz) (Fig. 1e). Overall, tNIR pulsed at different frequency exerted differential effects on cerebral blood flow in mice, with significant peaks occurring at two distinct tNIR frequency range: 60–80 Hz and 120–140 Hz. This demonstrates that specific frequency bands of near-infrared light indeed enhance the blood flow velocity at cerebral cortex. This effect is defined as a significant energy demand arising in cortical neuronal activities when the assemblies of cortical neurons resonate with specific frequencies of pulsed transcranial near-infrared light, necessitating increased blood flow to meet the heightened energy requirements[7,29–32]. In other words, the

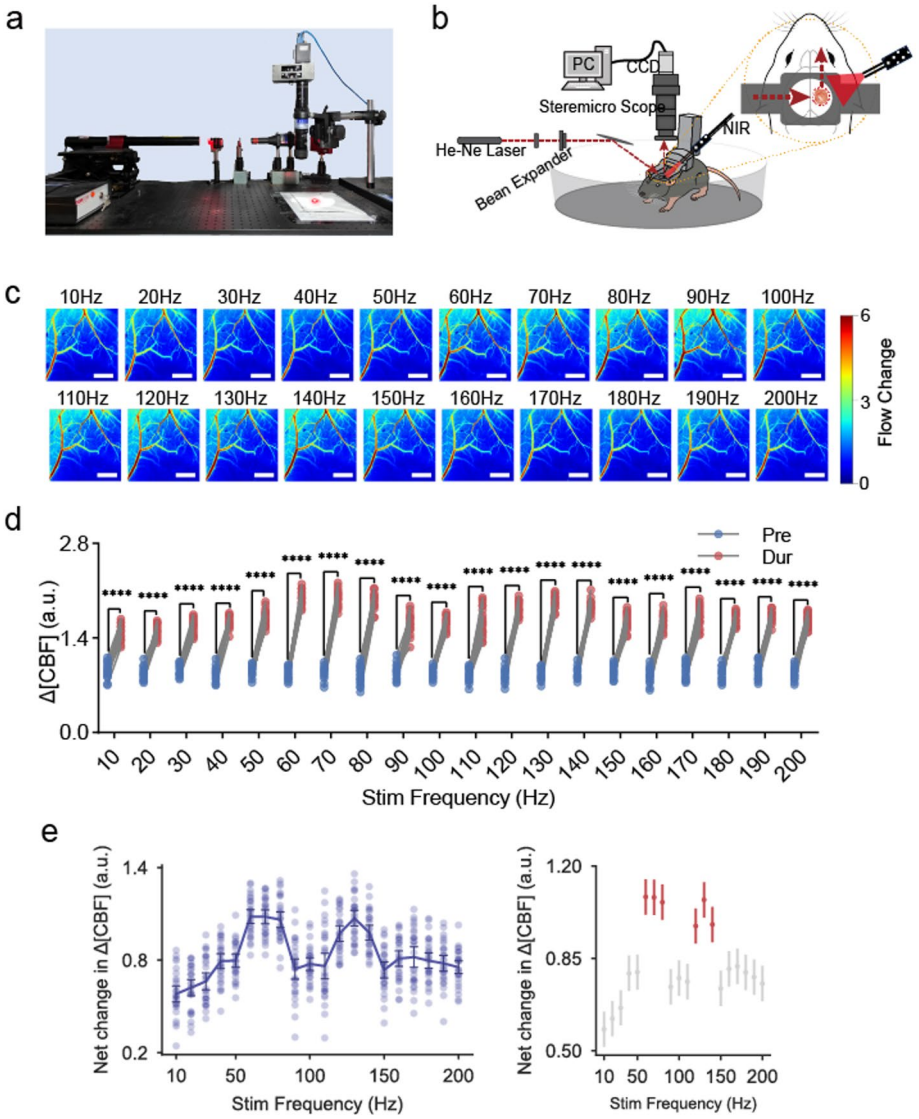


**Fig. 1**. Frequency responses of Δ[CBF] in cortex. (**a**) The setup for laser speckle contrast imaging used to analyze the dynamics of cerebral blood flow in the mouse cortex. (**b**) A schematic representation of the frequency response test, which involves incrementally altering the frequency of the external stimulation (tNIR) and continuously monitoring the neural response to pinpoint the frequency at which the response is markedly enhanced. (**c**) Pseudo-colored maps of CBF obtained through laser speckle contrast imaging under various pulsed tNIR frequencies. The white scale bar represents 0.65 mm, and the color bar indicates intensity levels. (**d**) Comparison of pre-tNIR Δ[CBF] and dur-tNIR Δ[CBF] at different tNIR frequencies (****$p < 0.0001$, two-sided paired t-test), a.u. arbitrary units. (**e**) Left, The frequency-response curvy for the net change in Δ[CBF]. A one-way repeated measures ANOVA was conducted on data from 30 observations per group from 10 mice to examine the impact of 20 different tNIR frequencies on Δ[CBF], revealing statistically significant differences ($F(19, 171) = 32.7156$, $P = 5.13 \times 10^{-47}$, mean ± s.e.m), a.u. arbitrary units. Right, tukey's honestly significant difference test was used to identify precisely which group means differed. Significance peaks among the groups are highlighted with red dots. Dots and error bars represent the means and 95% confidence intervals, respectively. a.u. arbitrary units.

occurrence of neural resonance phenomena can be inferred by examining the maximum responses of Δ[CBF] to specific frequencies of pulsed tNIR light.

To explore brain-state dependency, we conducted a new set of experiments in isoflurane-anesthetized mice ($n = 10$) using the same tNIR protocol (10–200 Hz). Frequency response curves for Δ[CBF] showed peaks at 60–80 Hz and 120–140 Hz, consistent with awake conditions, though with reduced amplitudes (~20–30%), suggesting that intrinsic frequency-dependent features persist despite altered neural activity states (Supplementary Fig. 1).

### Investigating neural resonance through the assessment of frequency responses of $\Delta[HbO_2]$ in cortex

In addition to assessing changes in cerebral cortical blood flow velocity, our investigation expanded to evaluate the concentration changes of oxygenated hemoglobin induced by different pulsed frequencies of near-infrared light. Employing intrinsic signal optical imaging (ISOI) (Fig. 2a-b), our aim was to ascertain whether specific frequencies could significantly enhance $\Delta[HbO_2]$. This exploration was grounded in the principle of neurovascular metabolic coupling, which posits that increased neural activity, and the resultant heightened energy demand, necessitates rapid metabolic responses[33–35]. Such responses manifest as the concentration of $\Delta[HbO_2]$ within the cortical vessels. Consequently, we monitored the fluctuations in $\Delta[HbO_2]$ concentrations, an essential oxygen-transporting component, across various tNIR frequencies. This approach allowed us to delineate the intricate relationship between cortical $\Delta[HbO_2]$ and neural activity.

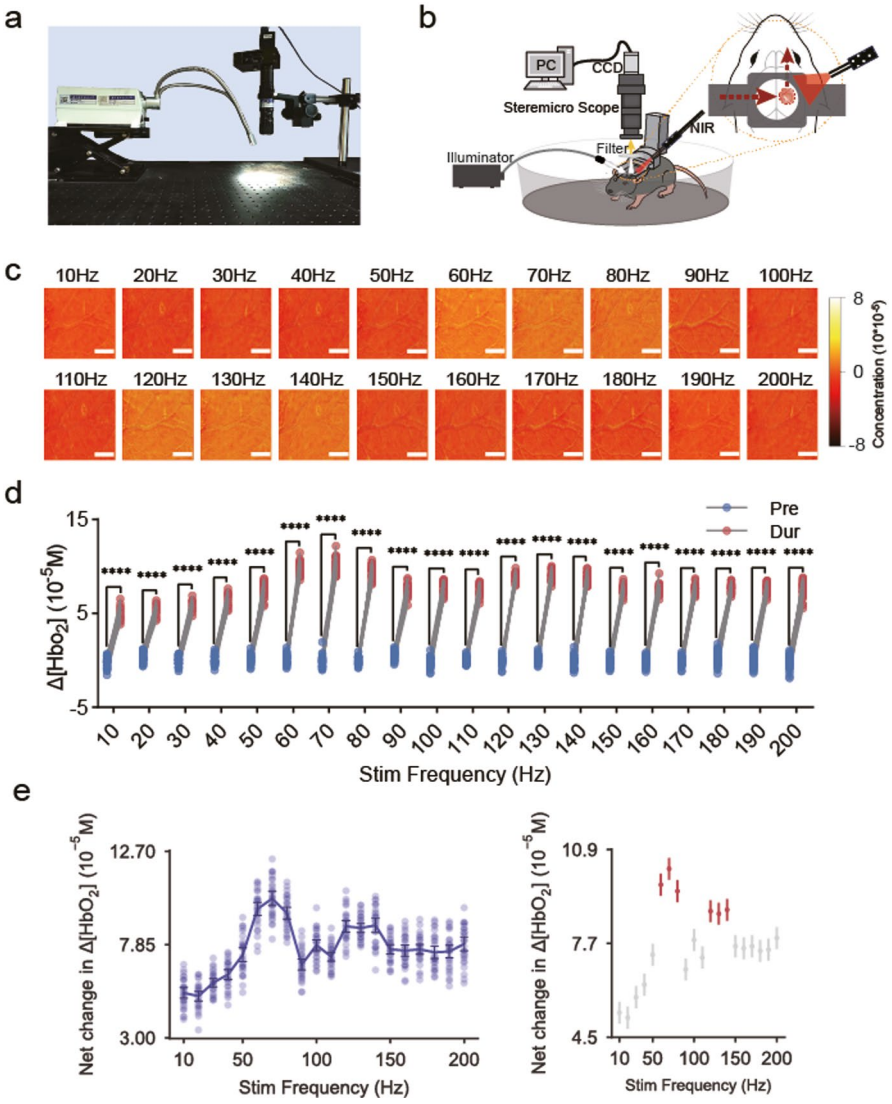


**Fig. 2**. Frequency responses of $\Delta[HbO_2]$ in cortex. (**a**) The setup for ISOI used to analyze the dynamics of cerebral blood flow in the mouse cortex. (**b**) In vivo ISOI was performed while mice were subjected to pulsed tNIR stimulation, allowing them to move freely on a rotatable plate. (**c**) Pseudo-colored maps of $\Delta[HbO_2]$ obtained through ISOI under various tNIR frequencies. The white scale bar represents 0.65 mm, and the color bar indicates concentration. (**d**) Comparison of Pre-$\Delta[HbO_2]$ and Dur-$\Delta[HbO_2]$ at different tNIR frequencies (****$p < 0.0001$, $n = 10$ mice, two-sided paired t-test). (**e**) Right, the frequency-response curvy for the net change in $\Delta[HbO_2]$. A one-way repeated measures ANOVA was conducted on data from 30 observations per group from 10 mice to examine the impact of 20 different tNIR frequencies on $\Delta[HbO_2]$, revealing statistically significant differences ($F(19, 171) = 88.2436$, $P = 6.53 \times 10^{-78}$, mean ± s.e.m). Left, tukey's honestly significant difference test was used to identify precisely which group means differed. Significance peaks among the groups are highlighted with red dots. Dots and error bars represent the means and 95% confidence intervals, respectively.

Experimental results indicate that, there was a significant increase in $\Delta[HbO_2]$ during tNIR stimulation (Dur-$\Delta[HbO_2]$) compared to the $\Delta[HbO_2]$ prior to tNIR stimulation (Pre-$\Delta[HbO_2]$) across all tNIR frequencies ranging from 10 to 200 Hz ($n=10$ mice, $P<0.0001$) (Fig. 2c,d). This indicates that tNIR pulses within the frequency range of 10–200 Hz are able to significantly enhance the $\Delta[HbO_2]$ of the mouse cerebral cortex. To further explore whether pulsed tNIR light modulation of $\Delta[HbO_2]$ is frequency-specific, we analyzed the relationship between $\Delta[HbO_2]$ and tNIR frequencies. It was found that $\Delta[HbO_2]$ exhibited a significant peak at tNIR frequencies of 60–80 Hz ($n=30$ observations per condition from 10 mice, $p<0.0001$ compared with 10–50 Hz, 90–110 Hz, and 150–200 Hz) (Fig. 2e), followed by a second significant peak at tNIR frequency range of 120–140 Hz ($n=10$ mice, $p<0.05$ compared with 10–50 Hz, 90–110 Hz, and 150–200 Hz) (Fig. 2e). The investigation into $\Delta[HbO_2]$ alterations within the mouse cortex revealed that $\Delta[HbO_2]$ exhibit frequency dependence, with significant increases in stimulus-induced $\Delta[HbO_2]$ observed within the 60–80 Hz and 120–140 Hz tNIR frequency range. This evidence suggests that specific tNIR frequency of transcranial near-infrared light not only substantially enhance blood flow velocity in the cerebral cortex but also significantly increase $\Delta[HbO_2]$ within cortical regions. This phenomenon can be interpreted as the cortical neurons requiring more energy to support enhanced neural activity when the collective cortical neuronal assemblies resonate with the specific frequencies of pulsed transcranial near-infrared light.

## Identifying resonance phenomena in cortex via electrocorticographic analysis

In addition to cortical $\Delta[CBF]$ and $\Delta[HbO_2]$, ECoG signals from the cortex more directly reflect the neural ensemble activity of the cortical surface, serving as a direct output of neural nuclei operating in a resonant state. By observing whether there are frequency-specific enhancements in the electrophysiological activity of ECoG under various tNIR frequencies stimulation, we aim to further explore the neural mechanisms underlying the resonance phenomenon. We also measured mouse ECoG signals (Fig. 3a-b) and analyzed the spectral power and sample entropy[36] (SamEn) of the ECoG signals to investigate cortical neuroelectrophysiological activity responses to different tNIR stimulation frequencies. The SamEn of ECoG reflects the richness of the electrocortical signals, with higher SamEn values indicating greater neural activity[37].

Specifically, we first calculated the average power spectral density (PSD) for electrodes PR1, PR2, and PR3 (located in the same region as the cranial window used in earlier experiments, Supplementary Fig. 4a) (Fig. 3c). To identify which EEG spectral frequency bands contain more stimulus-related information, we computed both the signal coefficient of variance[38] (sCV), quantifying trial-by-trial variability in spectral power due to stimulus-induced modulations, and the noise coefficient of variance (nCV), quantifying variability in spectral power across trials for the same stimulus. Our results revealed two sCV peaks during tNIR stimulation within 1–8 Hz and 110–120 Hz spectral frequency band (Fig. 3d), suggesting the need to focus on energy response variations in these bands across different stimulation frequencies. The ECoG signals power at 1–8 Hz and 110–120 Hz spectral frequency bands with varying tNIR frequencies. (1) For ECoG signals power at 1–8 Hz spectral frequency band, we observed significant increases in dur-tNIR spectral power (Dur-power) compared to the spectral power prior to tNIR stimulation (Pre-power) within the 60–80 Hz and 110–120 Hz tNIR frequency ranges ($n=10$ mice, $P<0.0001$) (Fig. 3e). By analyzing the relationship between the net changes in power and different tNIR frequencies, significant peaks of spectral power of ECoG signal were noted at 60–80 Hz and 110–120 Hz tNIR frequency band ($n=10$ mice, $p<0.0001$ compared with 10–50 Hz, 80–100 Hz, and 130–200 Hz) (Fig. 3f). (2) Regarding spectral power within 110–120 Hz spectral frequency band, we found significant peak in Dur-power within 110–140 Hz tNIR frequency range compared to Pre-power ($n=10$ mice, $P<0.0001$) (Fig. 3g). Analysis of the net changes in power within 110–120 Hz spectral frequency band and tNIR frequencies revealed a significant peak within the 120–140 Hz range ($n=10$ mice, $p<0.0001$ compared with other frequencies) (Fig. 3h).

We then analyzed the average sample entropy of the ECoG signal (channels PR1, PR2, PR3). Figure 3i displays the topography of SamEn of the ECoG signal under modulation by 810 nm tNIR light pulsed at different frequencies, with red in the color bar indicating high SamEn and blue indicating low SamEn. Results show that dur-tNIR SamEn (Dur-SamEn) significantly increased compared to the SamEn (Pre-SamEn) prior to tNIR stimulation within the 40–200 Hz tNIR frequency range ($n=10$ mice, $P<0.05$) (Fig. 3j). To further investigate the frequency-specific modulation effects of pulsed tNIR on SamEn of the ECoG signal, we analyzed the relationship between the net change in SamEn and tNIR frequencies. When stimulating the mouse brain with tNIR pulses at frequencies of 60–80 Hz and 120–140 Hz, two significant peaks were observed in the SamEn ($n=10$ mice, $p<0.0001$ compared with 10–50 Hz, 90–110 Hz, and 150–200 Hz) (Fig. 3k).

In accordance with the above results obtained from the two optical imaging analysis (discussed above), our frequency response tests revealed that spectral power and SamEn of the ECoG signals also exhibited frequency dependency. Consistent with the above changes in cerebral blood flow and oxygenated hemoglobin, neural electrical activity in the corresponding cortex also shows more significant enhancement within similar tNIR frequency bands (60–80 Hz and 120–140 Hz). This multi-dimensional evidence further corroborates the occurrence of resonance phenomena in the brain induced by tNIR.

## Identifying neural resonance in deep brain region (CA1)

Following the insights from the superficial brain region (cerebral cortex), including manifestations such as cerebral blood flow, oxygenated hemoglobin and cortical electroencephalographic signals, we delve deeper into whether individual neuronal spike potentials and collective neural local field potentials in deep brain regions are also induced to resonate under frequency response test. This exploration aims to extend our understanding of the resonance phenomenon from the superficial layers to the intricate dynamics of deep-brain neural nuclei. we delved into the potential resonance phenomena in the deeper brain region, specifically the CA1 area. For this, we recorded extracellular spiking activity and LFP from the CA1 region of mice (Fig. 4a).

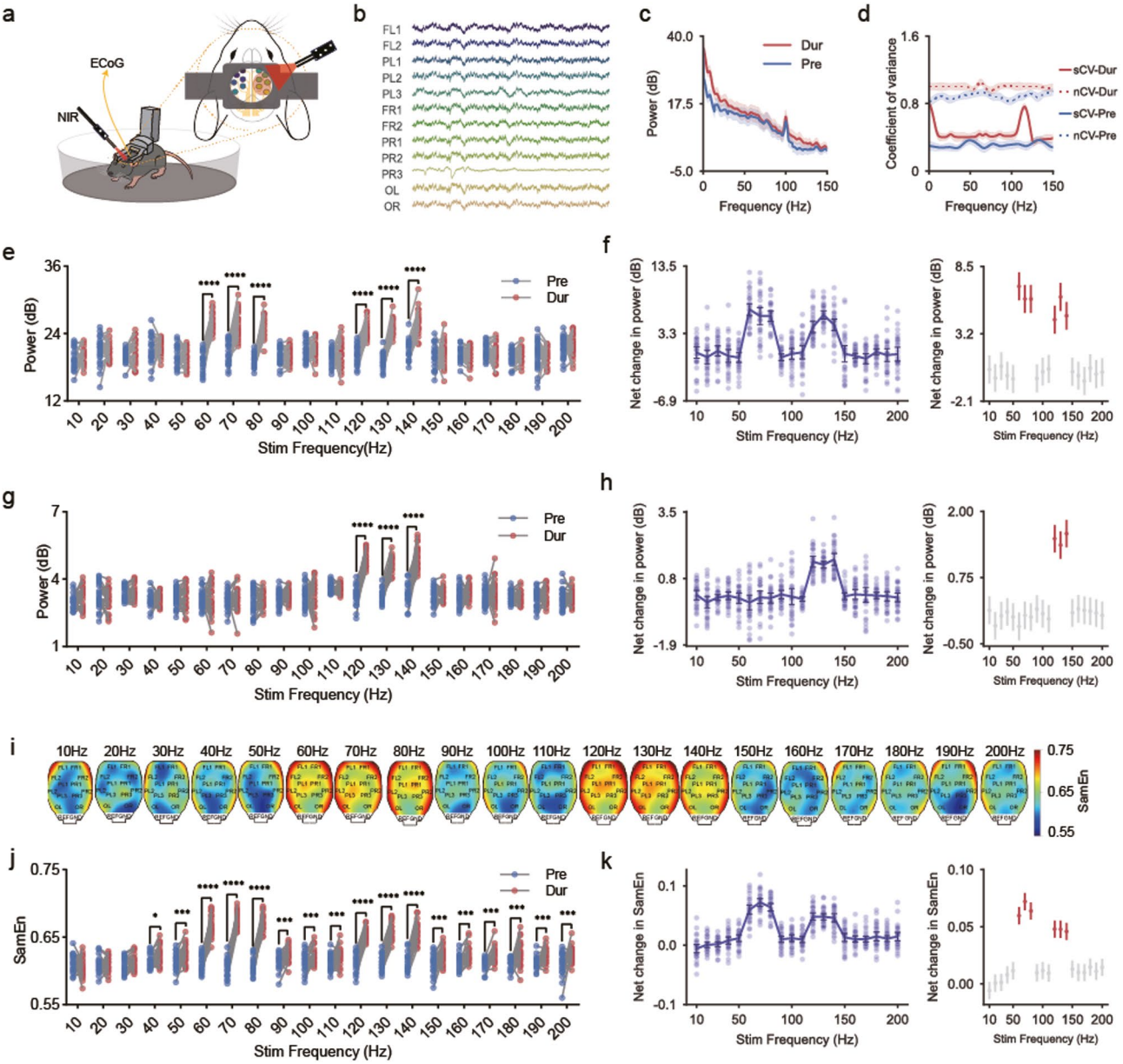


Initially, we explored the response pattern of multi-unit spiking activity (MUA) to different stimulation frequencies. The spike firing rate is indicative of stimulus-induced neuronal activity changes. Here, we present the trial-by-trial neural spike train raster plot for one multi-unit (Fig. 4b) and the trial-averaged peri-event time histogram (PETH) locked to the time of tNIR-stimulation for multi-unit (Fig. 4c). After analyzing the response of all mouse CA1 neuronal spike firing rates to different stimulation frequencies, we observed a significant increase in Dur-FR compared to Pre-FR only within the 120–130 Hz tNIR frequency range ($n = 8$ mice, 33 neurons, $P < 0.0001$) (Fig. 4d). This indicates that not all stimulation frequencies significantly alter the spiking activity in the mouse CA1 region. By analyzing the relationship between the changes in firing rate from baseline and different stimulation frequencies, a peak was noted within the 120–130 Hz tNIR frequency range ($n = 8$ mice, 33 neurons, $p < 0.01$) (Fig. 4e).

Additionally, we examined the LFP spectral power responses to different tNIR stimulation frequencies. We initially calculated the power spectral density (Fig. 4f) and found that the LFP at 1–10 Hz and 110–120 Hz exhibit particularly high sCV (Fig. 4g). But since the 1–8 Hz range exhibits high nCV, we inferred that the 110–120 Hz range contained more relevant information. Results show significant increases in Dur-power compared to Pre-power within the 60 Hz and 120-130 Hz tNIR frequency ranges ($n = 8$ mice, $P < 0.0001$) (Fig. 4h). Analyzing the net changes in LFP spectral power, significant peaks were observed at 60 Hz and 120-130 Hz ($n = 8$ mice, $p < 0.0001$ compared with 10–50 Hz, 70–110 Hz, and 140–200 Hz) (Fig. 4i).

In summary, our findings reveal that not all frequencies of pulsed tNIR significantly alter spiking activity and LFP spectral power in the CA1 region compared to baseline. Furthermore, by analyzing the changes in firing rate and LFP spectral power from baseline, we determined that stimulus-modulated neural responses in the CA1 were strongly influenced by specific stimulation frequencies. Preliminary evidence suggests that swept-frequency near-infrared light stimulation can induce resonance phenomena in deep brain structures. Local

◀**Fig. 3**. Frequency responses of ECoG signals in cortex. (**a**) The experimental setup for in vivo electrocorticographic signal recordings in freely moving mice subjected to tNIR stimulation on a rotatable plate. (**b**) An example of 12-channel ECoG activity recorded from various brain regions, with each trace color-coded to indicate specific electrode locations. (**c**) Compares the power spectral density during stimulation (red) and prior to stimulation (blue), averaged across channels PR1, PR2, and PR3, using tNIR at 810 nm, 50 mW/cm$^2$, with pulse frequencies from 10 to 200 Hz in 10 Hz increments, applied in a pseudo-randomized order ($n = 10$ mice). (**d**) The signal coefficient of variance (solid line) and the noise coefficient of variance (dashed line) of ECoGs as a function of frequency, with red and blue lines representing during and prior to stimulation, respectively, using the same tNIR parameters as in (**c**) ($n = 10$ mice). (**e**) Compares the pre-stimulation and during-stimulation power in the 1–8 Hz spectral frequency band at different tNIR frequencies (****$p < 0.0001$, $n = 10$ mice, two-sided paired t-test). (**f**) The frequency-response curve (right) shows the net power change in the 1–8 Hz band (one-way ANOVA, $F(19, 171) = 31.5911$, $P = 5.98 \times 10^{-46}$). Tukey's test (left) identified significant group differences, highlighted by red dots. Dots and error bars represent means and 95% confidence intervals, respectively. (**g**) Compares the pre-stimulation and during-stimulation power in the 110–120 Hz spectral frequency band at different tNIR frequencies. (**h**) The frequency-response curve (right) shows the net power change in the 110–120 Hz band (one-way ANOVA, $F(19, 171) = 30.6439$, $P = 3.54 \times 10^{-45}$). Tukey's test (left) identified significant group differences, highlighted by red dots. Dots and error bars represent means and 95% confidence intervals, respectively. **i** The topography of the sample entropy of the ECoG signal under modulation by tNIR at different frequencies. (**j**) Compares the pre-stimulation and during-stimulation SamEn at different tNIR frequencies. (**k**) The frequency-response curve (right) shows the net power change in average SamEn of the ECoG (channels PR1, PR2, PR3) (one-way ANOVA, $F(19, 171) = 66.8470$, $P = 8.63 \times 10^{-69}$. Tukey's test (left) identified significant group differences, highlighted by red dots. Dots and error bars represent means and 95% confidence intervals, respectively. mean ± s.e.m.

field potentials of deep-brain neural nuclei and the spike firing of individual neurons exhibit frequency-specific enhancements, indicating a profound impact of pulsed tNIR stimulation on deep cerebral regions.

### Computational modeling reveals neural resonance in neural network

To support our neural resonance hypothesis mechanistically, we conducted computational simulations by constructing a small-world neural network (nonlinear system) using the Strogatz-Watts method[39], with each neuron modeled by the two-dimensional map-based neuron model originally proposed by Rulkov[40]. An intrinsic signal was applied to 40% of nodes to represent intrinsic neural activity, while an external stimulation signal (10–250 Hz) was applied to all nodes to simulate external stimulation, mirroring our experimental design (Fig. 5a). Simulations demonstrated resonance-like phenomena, where external stimulation inputs enhance the network's response to the Intrinsic signal at optimal frequencies. The response factor Q (serves as a quantitative measure to assess the amplification of the intrinsic signal's response induced by the external stimulation applied across the network) exhibited peaks around 50–70 Hz and 140–160 Hz (Fig. 5b), qualitatively aligning with experimental peaks at 60–80 Hz and 120–140 Hz. This supports the presence of resonance-like dynamics, where external stimulation frequencies amplify intrinsic neural signals, producing dual peaks indicative of selective amplification. The minor offsets (~ 20 Hz in the higher peak) likely arise from the Rulkov model's discrete dynamics and normalized time scales, which do not fully capture the continuous, biologically detailed dynamics of tNIR-stimulated neural ensembles or specific photobiomodulation effects (e.g., CCO activation). This qualitative agreement strengthens our operational definition of neural resonance, inspired by stochastic resonance principles where specific external fluctuations maximize nonlinear system responses to a weak signal, as seen in excitable systems[41] and cortical networks[21,48].

## Discussion

The Food and Drug Administration (FDA) considers transcranial photobiomodulation to be a promising, cost-effective, and safe method for enhancing human cognitive abilities. Pulsed tNIR is capable of effectively penetrating the mouse skull, thereby reaching the central nervous system. This results in the induction of non-invasive neuromodulation effects through a photochemical mechanism involving mitochondrial chromophores, as opposed to the generation of heat. Previously successful applications of PBM in the treatment of various neurological disorders have demonstrated that among the light parameters, frequency plays a pivotal role, exhibiting a pronounced frequency-dependent therapeutic effect. The discovery of resonant phenomena within the nervous system suggests that it may operate as a resonant system. To test this hypothesis, a frequency response test was designed, in which a series of pulsed tNIR stimuli at varying frequencies (10–200 Hz, in 10 Hz steps) were applied to the mouse cerebral cortex, and neural responses were measured through multiple indicators (Δ[CBF], Δ[$HbO_2$], ECoG signals and spiking activity) to confirm the existence of neural resonance.

The relationship between Δ[$HbO_2$] and Δ[CBF] with neural activity is intricate and governed by the neurovascular coupling mechanism. This principle postulates that augmented neuronal activity precipitates an increase in blood flow, thereby ensuring the provision of additional oxygen and nutrients to active brain regions. This mechanism is of vital importance for the correct functioning of the brain and constitutes a fundamental element of brain metabolism. Consequently, by measuring the frequency response patterns of Δ[$HbO_2$] and Δ[CBF], it is possible to gain insight into the frequency response of neural activity. This approach provides a quantitative basis for understanding the dynamic interactions between pulsed tNIR stimulation and neural function. The results demonstrate that under tNIR stimulation at 60–80 Hz and 120–140 Hz, the response curves for the net change in Δ[$HbO_2$] exhibit two distinct peaks, indicating a clear frequency dependence and

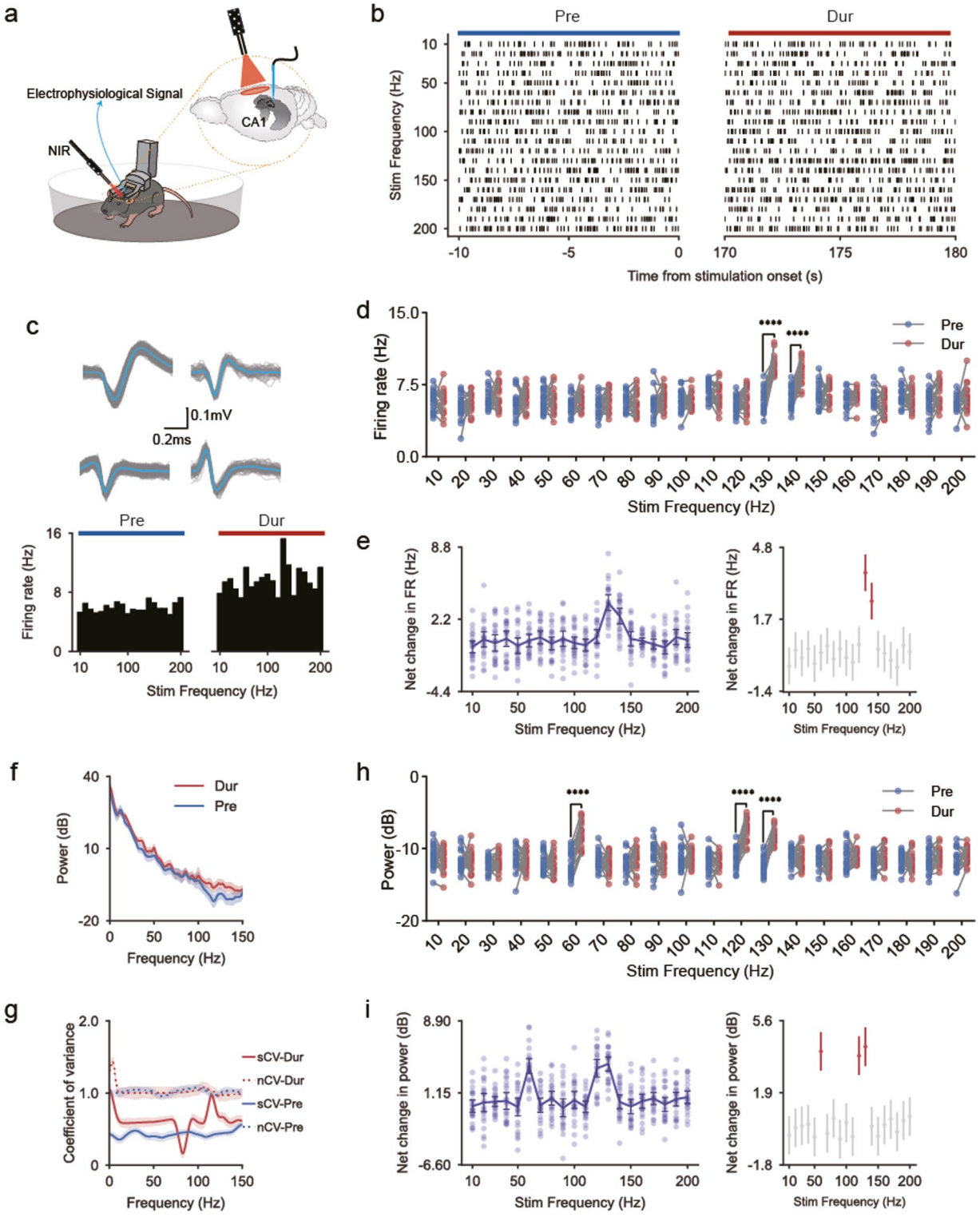


suggesting the presence of resonance phenomena. It is, however, noteworthy that a comparison of the pre- and post-$\Delta[HbO_2]$ measurements revealed that all pulse frequencies of tNIR significantly enhanced $\Delta[HbO_2]$. It is probable that this enhancement is the result of transcranial near-infrared (tNIR) radiation directly reaching the cortical region via an open cranial window, which causes vasodilation of cortical vessels, increasing local blood flow and thereby raising the concentration of oxygenated hemoglobin, leading to significant changes in $\Delta[HbO_2]$. Similar phenomena have been observed in studies of $\Delta$[CBF], which can be attributed to the same neurovascular metabolic coupling mechanism. In addition, a new set of experiments under isoflurane anesthesia revealed frequency response peaks at 60–80 Hz and 120–140 Hz for $\Delta$[CBF], consistent with awake mice, though with reduced amplitudes (~ 20–30%), likely due to suppressed high-frequency gamma oscillations as reported by Hudetz et al.[42]. We hypothesize that anesthesia primarily alters the activity state of neuronal populations without modifying the underlying structure, connectivity, or neuron types within the neural network. Consequently, the

◂**Fig. 4**. Frequency responses of extracellular spiking activity and LFP in CA1. (**a**) In vivo extracellular recordings was performed while mice were subjected to pulsed tNIR stimulation, allowing them to move freely on a rotatable plate. (**b**) An example of trial-by-trial raster plot locked to the time of tNIR-stimulation for one example multi-unit. (**c**) Top, waveforms of the action potentials recorded extracellularly. Bottom, trial-averaged peri-event time histogram. (**d**) Compares the pre-stimulation and during-stimulation FR at different tNIR frequencies (****$p < 0.0001$, $n = 8$ mice, two-sided paired t-test). **e** Right, the frequency-response curve shows the net FR change (one-way ANOVA, $F(19, 133) = 9.5591$, $P = 6.55 \times 10^{-17}$). Left, Tukey's test identified significant group differences, highlighted by red dots. Dots and error bars represent means and 95% confidence intervals, respectively. (**f**) The red line represents the LFP power spectral density during stimulation, while the blue line indicates the LFP power spectral density prior to stimulation. $n = 8$ mice. (**g**) The signal coefficient of variance (solid line) and the noise coefficient of variance (dashed line) of LFP as function of frequency, with red and blue lines representing during and prior to stimulation, respectively. $n = 8$ mice. (**h**) Comparison of pre-stimulation and during-stimulation power (110–120 Hz spectral frequency band) at different tNIR frequencies (****$p < 0.0001$, $n = 8$ mice, two-sided paired t-test). (**i**) Right, the frequency-response curvy for the net change in power ($F(19, 133) = 16.1017$, $P = 7.56 \times 10^{-26}$, mean ± s.e.m). Left, Tukey's test was applied to the data (right) to identify precisely which group means differed. Significance peaks among the groups are highlighted with red dots. Dots and error bars represent means and 95% confidence intervals, respectively. mean ± s.e.m.

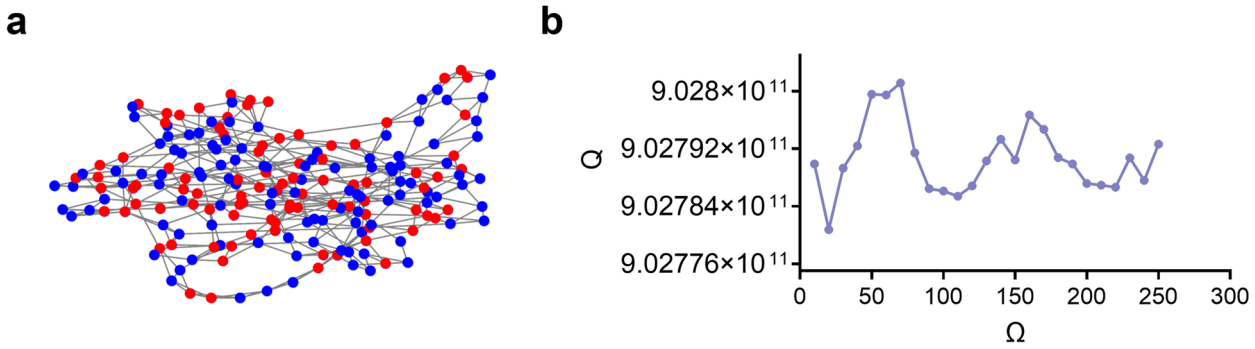


**Fig. 5**. Computational modeling of resonance-like phenomena. (**a**) Small-world neural network topology ($N = 200$ nodes, reconnection probability $p = 0.2$). Red dots: intrinsic signal nodes; red and blue dots: external stimulation signal nodes. (**b**) Simulated response factor Q vs. external stimulation frequency Ω (10–250 Hz), with peaks at 50–70 Hz and 140–160 Hz, qualitatively matching experimental peaks with minor offsets due to model simplifications.

frequency-dependent features of neural resonance, linked to the network's intrinsic frequencies determined by these structural properties, remain largely intact. This suggests that tNIR-induced effects combine resonance-like dynamics (tied to intrinsic network properties) with frequency-specific sensitivity, potentially driven by photochemical mechanisms (e.g., CCO activation) that are less sensitive to brain state changes. The consistency of peak frequencies across awake and anesthetized conditions supports our operational definition of neural resonance as selective amplification of intrinsic neural signals by external stimuli.

In addition to optical imaging techniques, we utilized neurophysiological methods to investigate neural resonance phenomena in the cerebral cortex. It was determined that the ECoG frequencies of 18 Hz and 110–120 Hz were the most informative with regard to the pulsed tNIR stimulus. The analysis of ECoG spectral power changes within these frequency ranges demonstrated comparable patterns to those observed in cortical blood flow and the concentration of oxygenated hemoglobin, with significant enhancements evident at 60–80 Hz and 120–140 Hz. This suggests that low-frequency ECoG responses can be validated using neurovascular metabolic coupling mechanisms. The enhancement of ECoG spectral power within the 110–120 Hz range was observed only at stimulation frequencies of 110–140 Hz, indicating that ECoG high-frequency components respond differently to pulsed tNIR stimuli compared to lower frequencies. Moreover, an examination of the sample entropy (SamEn) of ECoG data revealed a notable increase in complexity at 60–80 Hz and 120–140 Hz when subjected to pulsed tNIR stimulation. This suggests that these specific frequencies have a pronounced effect on the complexity of brain electrophysiological signals.

Furthermore, we investigated the impact of different frequencies of tNIR on the deeper brain region (CA1). It was observed that the application of tNIR at a frequency of 130–140 Hz resulted in a notable elevation in spike firing rates. Furthermore, LFP spectral power alterations within the 110–130 Hz range demonstrated considerable enhancements at 60 Hz and 120–130 Hz. This suggests that 810 nm tNIR is capable of effectively penetrating the skull and superficial regions of the brain[43], thereby influencing deep brain neural activity. In light of the areas targeted by pulsed tNIR and those captured in ECoG recordings, including the primary somatosensory, posterior parietal association, and visual regions, it is crucial to acknowledge the potential for

these regions to interact with CA1 through indirect neural projections or complex neural networks. It is therefore possible that tNIR exerts an indirect influence on CA1 neural activity by modulating these areas. To clarify the observed discrepancies in frequency responses between cortical and subcortical regions, we note that these are likely attributable to methodological differences in recording techniques and regional physiological variability, rather than frequency-dependent light penetration as initially speculated. Cortical ECoG recordings, using screw electrodes, capture local field potentials (LFPs) from large neuronal populations, reflecting synchronized activity across broad cortical areas, while CA1 recordings, using microelectrodes, detect spiking activity and LFPs from smaller, more localized neuronal populations (1–100 neurons), potentially reducing sensitivity to tNIR-induced effects. Additionally, regional differences in neuronal composition, connectivity, and intrinsic oscillatory properties between cortex and CA1 may contribute, with higher frequencies (120–130 Hz) potentially aligning better with CA1's intrinsic dynamics. Optical attenuation at 810 nm is primarily wavelength-dependent, with negligible frequency selectivity in the 60–130 Hz range, indicating that reduced CA1 responses at 60 Hz reflect network-specific dynamics. These findings support our neural resonance hypothesis, as consistent peak frequencies across regions suggest that tNIR amplifies intrinsic network signals, with variations reflecting regional network properties.

The concept of neural resonance, as observed with maximal tNIR-induced responses at 60–80 Hz and 120–140 Hz, is rooted in the nonlinear dynamics of neuronal networks. Douglass et al. demonstrated stochastic resonance (SR) in biological systems, showing that weak periodic signals can be amplified by optimal noise levels in nonlinear systems[20]. Similarly, Yu et al. showed SR in cortical inhibitory neuron models, with coherent oscillations when external stimulation aligns with intrinsic frequencies[48]. In our study, we propose that tNIR acts as an external stimulation input, amplifying intrinsic neural signals, with peak responses indicating neural resonance. Our computational model supports this, demonstrating SR-like dynamics with response factor Q peaks at 50–70 Hz and 140–160 Hz, qualitatively aligning with experimental peaks. The minor offsets (~ 20 Hz) likely arise from simplifications in the Rulkov model, such as its discrete dynamics and arbitrary time scales, which do not fully capture tNIR-specific effects like photochemical interactions. Additionally, these offsets may result from the use of continuous cosine signals ( $B\cos(\Omega\, n + \varphi_{\,i})$) as external stimuli in simulations, differing from the pulsed tNIR signals (rectangular waveforms) used in experiments, which may influence the frequency response dynamics in nonlinear systems. Nevertheless, this qualitative agreement strengthens our operational definition of neural resonance as selective amplification, analogous to classical resonance systems, but we acknowledge that deeper mechanistic insights require further exploration, such as through biophysically detailed models or optogenetic studies incorporating pulsed stimulation. Overall, the two phenomena of stochastic resonance and neural resonance reveal the complexity and environmental adaptability of neural system dynamics from different perspectives. Stochastic resonance demonstrates that moderate noise can optimize the response of neural systems to weak signals, which is an important mechanism of environmental adaptation; and the phenomenon of neural resonance discovered in this paper reveals that the nervous system can actively amplify specific information by matching the frequency of external stimuli. Future research can further explore the physiological mechanisms and clinical applications of neural resonance, expanding our understanding of the dynamic principles of the nervous system.

## Conclusion

The findings of this study demonstrate a discernible pattern: both the cerebral cortex and the CA1 region exhibit markedly elevated responses within the frequency range of specific tNIR pulses. The observed frequency-dependent neural responses indicate the presence of an underlying resonance phenomenon within the nervous system. This phenomenon has been observed in a variety of systems, including mechanical, electronic, and molecular systems, and occurs when an external stimulus resonates with the intrinsic frequency of the system. Neuronal assemblies operate at resonant frequencies under normal conditions, responding to the intrinsic properties of the nervous system and providing the basis for the execution of normal physiological functions. The discovery of this resonance phenomenon provides insight into the effectiveness of specific frequencies and offers theoretical guidance for the selection of specific optical stimulation frequency parameters. In the future, it will provide a new theoretical framework and mechanism orientation for the clinical application of LLLT physical stimulation neuromodulation intervention for major brain diseases.

## Method and materials

### Animal

All experimental procedures were conducted in accordance with the guidelines set by the Boston University Animal Care and Use Committee and were approved by the Institutional Animal Care and Use Committee of Nanjing Medical University (Approval No. IACUC-2212014). The study is reported in accordance with the ARRIVE guidelines for animal research (https://arriveguidelines.org). Adult male mice (C57/BL6, aged between 2 and 3 months and weighing 25–30 g) were used in experiments. The mice were purchased from Qinglongshan Animal Center (Nanjing, China). They were fed autoclaved food and water ad libitum and housed in polypropylene cages (370 × 260 × 170 mm, five mice per cage) with corncob bedding on a 12-hour light/dark cycle in a specific pathogen–free facility. The ambient conditions were controlled at a temperature of 20˚C to 24˚C and a humidity level between 50 and 60%. Post-surgery, each mouse was individually housed. Prior to the commencement of experiments, the mice underwent an acclimatization process to a head-fixed condition. They were allowed to freely run on a rotatable plate for a minimum of 30 min daily, lasting 2 to 3 days. All experiments were conducted during the daytime hours.

A total of 38 adult male C57BL/6 mice were used in this study. The mice were divided into three groups for different recording techniques: 20 mice for LSCI (10 for awake vs. 10 for anesthesia) and ISOI, 10 mice for electrocorticography (ECoG) recording, and 8 mice for extracellular recording in the hippocampal CA1 region.

All mice received transcranial near-infrared light (tNIR) stimulation with the same parameters: wavelength of 810 nm, intensity of 50 $mW/cm^2$, and pulse frequencies ranging from 10 to 200 Hz in 10 Hz increments. The order of stimulation frequencies was pseudo-randomized within each session.

For the LSCI and ISOI group, the same 10 mice underwent both techniques to measure cerebral blood flow (CBF) and oxygenated hemoglobin concentration ($HbO_2$) changes, respectively. The recordings were performed in separate sessions to avoid interference.

In the ECoG group, 10 mice were implanted with flexible electrode arrays covering the left and right cerebral cortices. Each mouse underwent multiple recording sessions with different tNIR stimulation frequencies.

For the hippocampal CA1 group, 8 mice were implanted with microelectrode arrays targeting the CA1 region for extracellular recording of single-unit activity and local field potentials (LFPs). These mice also received tNIR stimulation with various frequencies during recording sessions.

## Experimental design and trial structure

Each experimental session consisted of 20 trials, with each trial comprising three phases: a 180-second pre-tNIR period, a 180-second during-tNIR period, and a 180-second rest phase (Supplementary Fig. 2). The initial 180 s of pre-tNIR in each experiment were consistent across all trials. All parameters stabilized within 90 s after the onset of stimulation and returned to baseline levels at least 60 s following the cessation of stimulation (Supplementary Fig. 3). To ensure the reliability of the data, we selected the final 10 s (from 170 to 180 s) of the pre-tNIR baseline as control data and the last 10 s (from 170 to 180 s) of the during-tNIR phase as experimental data. To minimize the potential for signal variations due to the tNIR frequency of individual trials rather than between trials, the order of trials within each session was randomized.

## Craniotomy procedure

To measure changes in cerebral blood flow and oxygenated hemoglobin for optical imaging, a craniotomy was performed. The procedure was conducted on the same day as the tNIR stimulation experiments to minimize potential interference from scar tissue formation or tissue recovery processes. Under 5% isoflurane anesthesia, the mouse's head was secured in a stereotaxic apparatus. The scalp was disinfected with iodine and incised to expose the skull. Connective tissues were carefully removed, and a handheld drill (RWD, China) was used to create a 3 mm diameter cranial window (ML: -1.2, AP: 5.2) to expose the underlying blood vessels, avoiding damage to vasculature. The entire cranial window was covered by the tNIR irradiation area during experiments (Figs. 1b and 2b, Supplementary Fig. 4a).

## Laser speckle contrast imaging

The brain blood flow velocity maps were acquired using a Laser Speckle Contrast Imaging platform (Fig. 2a) with the Gaussian Kernel Laser Speckle Contrast Analysis (gLASCA) algorithm[44]. A 632.8 nm laser (HeNe Laser, HNL150L-EC, Thorlabs, USA) was passed through a beam expander (Thorlabs, GBE15-A) and collimator, producing a parallel collimated light source, directed to the mouse head via a reflector (Hengyang Optics, China). Scattered light was magnified by an optical tube (Navitar, 1–50486 A 12X Zoom) and captured by a CCD camera (PointGrey, GS3-U3-51S5M-C) at 30 frames per second. To prevent crosstalk between tNIR stimulation (810 nm) and LSCI measurements (632.8 nm), within the 180-second tNIR stimulation phase (dur-stim), the tNIR stimulation was applied for 170 s, and the final 10 s were used exclusively for LSCI data collection without tNIR illumination. This temporal separation ensured no interference between stimulation and measurement wavelengths.

In vivo recordings were conducted while mice were allowed to move freely on a rotatable plate. Three recording trials, each lasting 540 s, were performed. The global area's average value was computed as the relative change in mice cerebral blood flow velocity.

## Experiments in anesthetized mice

A new set of experiments was conducted under isoflurane anesthesia ($n = 10$ mice) to assess the brain-state dependency of frequency response peaks. The same tNIR stimulation protocol (810 nm, 50 $mW/cm^2$, 10–200 Hz in 10 Hz increments) and LSCI methods were applied as in awake animals. Recordings followed the same trial structure (180 s pre-tNIR, 180 s dur-tNIR, 180 s rest), with data from the final 10 s of pre- and dur-tNIR phases analyzed to compare frequency response curves (Supplementary Fig. 1).

## Intrinsic signal optical imaging

ISOI technology reflects physiological metabolic changes in the brain cortex. Utilizing our ISOI analysis platform (Fig. 3a), changes in oxygenated hemoglobin concentration were measured based on the Beer-Lambert law. The system included a dual gooseneck cold light source (Olympus, LG-PS2), a set of six bandpass filters (FB450-10, CWL = 450 nm; FB470-10, CWL = 470 nm; FB500-10, CWL = 500 nm; FB550-10, CWL = 550 nm; FB570-10, CWL = 570 nm; FB600-10, CWL = 600 nm; all from Thorlabs, USA), an optical lens (Navitar, 1–50486 A 12X Zoom), a CCD camera (PointGrey, GS3-U3-51S5M-C), and system acquisition software. Broadband light from the cold light source illuminated the mouse brain, and reflected light passed through the filter set and optical lens to the CCD camera, capturing images at 30 frames per second across the six wavelengths sequentially. Recordings were conducted with mice freely moving on a rotatable plate, with four trials, each lasting 540 s.

## ECoG flexible electrode array

The electrocorticography (ECoG) flexible electrode array comprised 14 channels, fabricated using flexible electrode printing technology, with specific coordinates relative to the Lambda point: FL1 (ML: −1.2, AP: 1.2), FL2 (ML: −2.5, AP: −0.2), PL1 (ML: −1.2, AP: −1.1), PL2 (ML: −3.2, AP: −2.0), PL3 (ML: −1.2, AP: −2.9), OL (ML: −2.5, AP: −3.8), REF (ML: −1.2, AP: −5.8), FR1 (ML: 1.2, AP: 1.2), FR2 (ML: 2.5, AP: −0.2), PR1 (ML: 1.2, AP: −1.1), PR2 (ML: 3.2, AP: −2.0), PR3 (ML: 1.2, AP: −2.9), OR (ML: 2.5, AP: −3.8), GND (ML: 1.2, AP: −5.8). Each channel featured a circular electrode hole (0.7 mm diameter) surrounded by a 0.3 mm copper pad, enabling connection to Samtec connectors via soldering for interfacing with a headstage. To implant the electrode array for ECoG recordings, a surgical procedure was performed on the same day as the transcranial near-infrared (tNIR) stimulation experiments to minimize potential interference from scar tissue formation or tissue recovery processes. Under 5% isoflurane anesthesia, the mouse's head was secured in a stereotaxic apparatus. The scalp was disinfected with iodine and incised to expose the skull. Connective tissues were carefully removed, and a handheld drill (RWD, China) was used to create 14 holes in the skull at the specified coordinates, avoiding damage to the underlying dura mater. The flexible electrode array was then placed on the skull, and stainless steel screws (0.7 mm diameter) were inserted through the array's holes into the drilled cranial holes without penetrating the dura. Twelve electrodes corresponded to distinct cortical regions, while the reference (REF) and ground (GND) electrodes were positioned over the cerebellum (Supplementary Fig. 4b). After electrode implantation, mice were allowed to recover from anesthesia before tNIR stimulation experiments commenced.

## ECoG recording

ECoG signals were captured from the cerebral cortex using 14-channel stainless steel flexible recording arrays. The electrode channels included FL1, FL2, PL1, PL2, PL3, OL, REF, FR1, FR2, PR1, PR2, PR3, OR, and GND, as detailed in the ECoG Flexible Electrode Array section. Raw signals were sampled at 30 kHz, while ECoG signals were sampled at 2 kHz. During data recording, a 250 Hz low-pass filter was utilized, and a band-stop filter was applied to remove 50 Hz power line noise. Signal acquisition and preprocessing were conducted using the Cerebus multi-channel neural signal recording system (Blackrock Microsystems, USA). To ensure the integrity of the data and minimize external interference, data collection was carried out with the head-fixed, awake animals freely running on a carbon fiber rotatable plate.

## Electrode implantation

For in vivo extracellular recording, four bundles of electrodes were fabricated, each containing four Teflon-insulated tungsten microwires. Before surgical implantation, the electrodes were tested for short circuits and impedance. Under isoflurane anesthesia, a craniotomy was performed over the CA1 recording regions. The 8 recording electrodes were then carefully inserted into the CA1 region based on stereotaxic coordinates (from bregma: AP: −1.95 mm, ML: 1.5 mm, DV: −1.5 mm). Two silver wires, attached to a skull screw, served as the ground and reference. Finally, the electrodes and a metal plate for head fixation were secured to the skull with dental cement. The mice underwent a 3-day habituation to the head-fixation setup, with daily sessions lasting 30 min, before the start of experiments.

## Electrophysiological recording

Two weeks after recovery from electrode implantation, in vivo recording sessions were conducted. Mice were allowed to move freely on a rotatable plate during these sessions. Five recording sessions, each lasting 3 min, were carried out. Spike data were sampled at 30 kS/s with a 250 ~ 5k Hz bandpass filter, while local field potential (LFP) data were sampled at 2 kS/s with a 250 Hz lowpass filter, using the CerePlex Direct system (Blackrock Microsystems, USA).

## Spike analysis

Baseline activity was recorded for 10 s before stimulation. Only stable spike trains were subsequently recorded and analyzed. Single units were sorted offline using the K-Means Scan method (Plexon Offline Sorter). Units with over 5% of spikes within a 3 ms refractory period in the autocorrelation histogram were excluded to ensure good unit isolation. In total, 26 single units were obtained from 8 mice. Our focus was on estimating the changes in population firing rates across all channels (as opposed to single-unit activities), hence, the firing rates from all units were combined to represent the multi-unit firing rates for each trial[45,46].

## Verification of electrode site

To ensure accurate placement of microelectrodes in the mouse brain, Nissl staining was conducted post experimentally. After neural recording sessions, mice were deeply anesthetized and perfused transcardially with 0.9% NaCl followed by 4% paraformaldehyde (PFA). The brains were then extracted and post-fixed in 4% PFA for 24 h, followed by cryoprotection in 30% sucrose solution for 48 h. Coronal sections of 50 μm thickness were prepared using a Leica CM1520 freezing microtome. The sections were air-dried, rehydrated, and stained with 0.1% cresyl violet acetate for 6 min at room temperature. After rinsing in water, the sections were dehydrated through a graded series of alcohol (70%, 95%, 100% x 2), cleared in xylene, and cover-slipped with Permount. Fluorescence Microscopy (Olympus, BX51WI) was utilized to visualize electrode tracks and record the final stereotaxic coordinates of electrode positions within targeted brain regions. This staining process followed standard histological protocols for Nissl staining in neural tissues.

*Near-Infrared (NIR) neuromodulation system*

To provide a stable and adjustable light source, a near-infrared (NIR) neuromodulation system was designed, comprising an light-emitting diode (LED) constant current driver module, a microcontroller module, a display

screen module, and a keypad module. The LED constant current driver module regulates the parameters of the LED light source via PWM signals from the microcontroller. The microcontroller module generates PWM signals, allowing modulation of frequency, duty cycle, and time intervals. The display screen module shows real-time data on the modulation of the LED light source, including frequency, stimulation duration, and duty cycle. The keypad module is used for setting experimental parameters like modulation time, power, and frequency. The NIR light is transmitted through custom-designed optical fibers.'

### tNIR stimulation setup and parameters

The continuous pulsed tNIR setup features a central wavelength of 810 nm with a half-maximum bandwidth of 40 nm, and the diameter of the tNIR irradiation area is set to 1 cm. In terms of stimulation parameters, the LED power density is regulated at 50 mW/cm$^2$ using a customized LED driver circuit. This regulation is based on studies indicating that higher energy levels could lead to the heating effects of the light[9,47], which we aim to avoid to ensure safe and effective stimulation. The experiment includes 20 groups, with the pulsed tNIR working at frequencies ranging from 10 to 200 Hz, in 10 Hz increments (Supplementary Fig. 5), controlled by the customized LED driver circuit.

*Computational modeling of neural resonance*

The computational modeling of neural resonance was conducted to investigate the effects of vibrational resonance in a small-world neural network using the two-dimensional map, a discrete-time nonlinear dynamical model. The network consisted of $N = 200$ neurons, constructed using the Watts–Strogatz model[39] with an initial degree $k = 4$ and a reconnection probability $p = 0.2$, yielding a topology characterized by high clustering and short average path lengths. Each neuron's dynamics were governed by the two-dimensional map equations:

$$x_{i,n+1} = \alpha_i/(1 + x_{i,n}^2) + y_{i,n} + I_{intrinsic} + I_{external} + I_{i,n}^{syn}(x_{i,n})$$
$$y_{i,n+1} = y_{i,n} - \sigma\, x_{i,n} - \beta_i$$

where $x_{i,n}$ and $y_{i,n}$ represent the fast (membrane potential) and slow (recovery) variables of neuron i at time step n, respectively. The parameter $\alpha_i = 4.0$ controlled the nonlinear dynamics, $\sigma = 0.001$ governed the slow variable evolution, and $\beta_i = -1.0$ acted as a bias. The synaptic coupling term $I_{i,n}^{syn}(x_{i,n}) = \epsilon \sum_j C(i,j)(x_{j,n} - x_{i,n})$ incorporated network interactions, with $\epsilon = 0.01$ as the coupling strength and $(C(i,j))$ as the adjacency matrix derived from the small-world network.

To study neural resonance, two types of signals were introduced: an intrinsic signal (generated within a subset of neurons in the small-world neural network) and an external stimulation signal (applied to all neurons in the network). The intrinsic signal, $I_{intrinsic} = A\cos(\omega\, n)$, with amplitude $A = 0.01$ and frequency $\omega = 10$ Hz, was applied to a subset of neurons with a probability 0.4. The external signal, $I_{external} = B\cos(\Omega\, n + \varphi_i)$, with amplitude $B = 1.0$ and frequency $\Omega$ varying from 10 to 250 Hz, was applied to all neurons, where $\varphi_i$ represented a random phase for each neuron. The simulation employed a time step $dt = 0.001$ s (1 kHz sampling rate), and the total simulation duration was T = 10,000 steps (10 s).

The network dynamics were simulated using a custom Python implementation with NumPy and NetworkX libraries. For each external signal frequency value, the system was initialized with random states for x and y, and the equations were iterated over time. The response to the intrinsic signal was quantified using the response factor Q, defined as:

$$Q = P_{out}(\omega)/P_{in}(\omega)$$

where $P_{out}(\omega)$ is the power spectral density of the fast variable x at frequency $\omega$, computed via Fast Fourier Transform (FFT), and $P_{in}(\omega) = A^2/2$ represent the theoretical power of the intrinsic signal with amplitudes. The mean response factor Q across all neurons was calculated to assess the network-level resonance. This response factor serves as a quantitative measure to assess the amplification of the intrinsic signal's response induced by the external stimulation applied across the network. Visualization included time series of x, network topology, frequency spectra, and Q as a function of $\Omega$, generated using Matplotlib. Parameters were adjustable to explore resonance phenomena under varying conditions, with results reproducible via a fixed random seed.

*Statistics*

Results were deemed statistically significant if the P-value was less than 0.05. Prior to further analysis, all data were subjected to the one-sample Kolmogorov–Smirnov test to assess normality. Paired one-tailed t-test was used to compare two groups. Statistical differences between various stimulation parameters were evaluated using one-way repeated-measures ANOVA ($p < 0.05$), supplemented by Tukey's honestly significant difference (HSD) test for post hoc multiple comparisons. The adjusted P values reported for ANOVAs are the most conservative lower bound adjustments, as calculated using Python. Error bars in the data represent the standard error of the mean (s.e.m.). Data analysis was conducted using custom Python scripts and GraphPad Prism version 8 (GraphPad Software, San Diego, CA, United States).

## Data availability

The data that support the findings of this study are available upon reasonable request.

## Code availability

The Python code used for simulating vibrational resonance in a small-world neural network with the two-di-

mensional map model is publicly available at https://osf.io/bk6ew/.

Received: 29 December 2024; Accepted: 19 September 2025
Published online: 04 December 2025

## References

1. Salehpour, F. et al. Brain photobiomodulation therapy: A narrative review. *Mol. Neurobiol.* **55** (8), 6601–6636 (2018).
2. Dompe, C. et al. Photobiomodulation-underlying mechanism and clinical applications. *J. Clin. Med.* **9** (6), 17 (2020).
3. Topaloglu, N. & Bakay, E. Mechanistic approaches to the light-induced neural cell differentiation: Photobiomodulation vs low-dose photodynamic therapy. *Photodiagnosis Photodyn Ther.* ;**37**. (2022).
4. Chung, H. et al. The nuts and bolts of low-level laser (light) therapy. *Ann. Biomed. Eng.* **40** (2), 516–533 (2012).
5. Hamblin, M. R. Shining light on the head: Photobiomodulation for brain disorders. *BBA Clin.* **6**, 113–124 (2016).
6. Sleep, S. L., Skelly, D., Love, R. M. & George, R. Bioenergetics of photobiomodulated osteoblast mitochondrial cells derived from human pulp stem cells: Systematic review. *Lasers Med. Sci.* **37** (3), 1843–1853 (2022).
7. Wang, X. et al. Up-regulation of cerebral cytochrome-c-oxidase and hemodynamics by transcranial infrared laser stimulation: A broadband near-infrared spectroscopy study. *J. Cereb. Blood Flow. Metab.* **37** (12), 3789–3802 (2017).
8. Wu, Q. et al. Low-level laser therapy for closed-head traumatic brain injury in mice: Effect of different wavelengths. *Lasers Surg. Med.* **44** (3), 218–226 (2012).
9. Ando, T. et al. Comparison of therapeutic effects between pulsed and continuous wave 810-nm wavelength laser irradiation for traumatic brain injury in mice. *PLoS ONE.* **6** (10), e26212 (2011).
10. Morries, L. D., Cassano, P. & Henderson, T. A. Treatments for traumatic brain injury with emphasis on transcranial near-infrared laser phototherapy. *Neuropsychiatr. Dis. Treat.* **11**, 2159–2175 (2015).
11. Salehpour, F., Rasta, S. H., Mohaddes, G., Sadigh-Eteghad, S. & Salarirad, S. Therapeutic effects of 10-Hz pulsed wave lasers in rat depression model: A comparison between near-infrared and red wavelengths. *Lasers Surg. Med.* **48** (7), 695–705 (2016).
12. Tao, L. et al. Microglia modulation with 1070-nm light attenuates Aβ burden and cognitive impairment in alzheimer's disease mouse model. *Light Sci. Appl.* **10** (1), 179 (2021).
13. Salehpour, F. et al. Transcranial low-level laser therapy improves brain mitochondrial function and cognitive impairment in D-galactose-induced aging mice. *Neurobiol. Aging.* **58**, 140–150 (2017).
14. Salehpour, F. et al. Near-infrared photobiomodulation combined with coenzyme Q(10) for depression in a mouse model of restraint stress: Reduction in oxidative stress, neuroinflammation, and apoptosis. *Brain Res. Bull.* **144**, 213–222 (2019).
15. Salehpour, F. & Rasta, S. H. The potential of transcranial photobiomodulation therapy for treatment of major depressive disorder. *Rev. Neurosci.* **28** (4), 441–453 (2017).
16. Lapchak, P. A., Salgado, K. F., Chao, C. H. & Zivin, J. A. Transcranial near-infrared light therapy improves motor function following embolic strokes in rabbits: An extended therapeutic window study using continuous and pulse frequency delivery modes. *Neuroscience* **148** (4), 907–914 (2007).
17. Wu, X. et al. Pulsed light irradiation improves behavioral outcome in a rat model of chronic mild stress. *Lasers Surg. Med.* **44** (3), 227–232 (2012).
18. Zomorrodi, R., Loheswaran, G., Pushparaj, A. & Lim, L. Pulsed near infrared transcranial and intranasal photobiomodulation significantly modulates neural oscillations: A pilot exploratory study. *Sci. Rep.* **9** (1), 6309 (2019).
19. Zomorrodi, R., Loheswaran, G., Pushparaj, A. & Lim, L. Modulation of neural Oscillation power spectral density with transcranial photobiomodulation. *Brain Stimul.* **12** (2), 457–458 (2019).
20. Douglass, J. K., Wilkens, L., Pantazelou, E. & Moss, F. Noise enhancement of information transfer in crayfish mechanoreceptors by stochastic resonance. *Nature* **365** (6444), 337–340 (1993).
21. Noda, T. & Takahashi, H. Stochastic resonance in sparse neuronal network: Functional role of ongoing activity to detect weak sensory input in awake auditory cortex of rat. *Cereb. Cortex.* **34** (1), bhad428 (2024).
22. De Taboada, L. et al. Transcranial laser therapy attenuates amyloid-β peptide neuropathology in amyloid-β protein precursor Transgenic mice. *J. Alzheimers Dis.* **23** (3), 521–535 (2011).
23. Peoples, C. et al. Photobiomodulation enhances nigral dopaminergic cell survival in a chronic MPTP mouse model of parkinson's disease. *Parkinsonism Relat. Disord.* **18** (5), 469–476 (2012).
24. Konstantinovic, L. M. et al. Transcranial application of near-infrared low-level laser can modulate cortical excitability. *Lasers Surg. Med.* **45** (10), 648–653 (2013).
25. Baker, W. B. et al. Neurovascular coupling varies with level of global cerebral ischemia in a rat model. *J. Cereb. Blood Flow. Metab.* **33** (1), 97–105 (2013).
26. Senarathna, J., Rege, A., Li, N. & Thakor, N. V. Laser speckle contrast imaging: Theory, instrumentation and applications. *IEEE Rev. Biomed. Eng.* **6**, 99–110 (2013).
27. Briers, D. et al. Laser speckle contrast imaging: Theoretical and practical limitations. *J. Biomed. Opt.* **18** (6), 066018 (2013).
28. Boas, D. A. & Dunn, A. K. Laser speckle contrast imaging in biomedical optics. *J. Biomed. Opt.* **15**(1) (2010).
29. Miller, A. et al. Spatially resolved metabolomics and isotope tracing reveal dynamic metabolic responses of dentate granule neurons with acute stimulation. *Nat. Metab.* **5** (10), 1820–1835 (2023).
30. Fox, P. T., Raichle, M. E., Mintun, M. A. & Dence, C. Nonoxidative glucose consumption during focal physiologic neural activity. *Science* **241** (4864), 462–464 (1988).
31. Attwell, D. et al. Glial and neuronal control of brain blood flow. *Nature* **468** (7321), 232–243 (2010).
32. Bonvento, G. & Bolanos, J. P. Astrocyte-neuron metabolic cooperation shapes brain activity. *Cell. Metab.* **33** (8), 1546–1564 (2021).
33. Buxton, R. B. & Frank, L. R. A model for the coupling between cerebral blood flow and oxygen metabolism during neural stimulation. *J. Cereb. Blood Flow. Metab.* **17** (1), 64–72 (1997).
34. Hosford, P. S. & Gourine, A. V. What is the key mediator of the neurovascular coupling response? *Neurosci. Biobehav Rev.* **96**, 174–181 (2019).
35. Iadecola, C. The neurovascular unit coming of age: A journey through neurovascular coupling in health and disease. *Neuron* **96** (1), 17–42 (2017).
36. Richman, J. S. & Moorman, J. R. Physiological time-series analysis using approximate entropy and sample entropy. *Am. J. Physiol. Heart Circ. Physiol.* **278** (6), H2039–H2049 (2000).
37. Carhart-Harris, R. L. et al. The entropic brain: A theory of conscious states informed by neuroimaging research with psychedelic drugs. *Front. Hum. Neurosci.* **8**, 20 (2014).
38. Belitski, A. et al. Low-frequency local field potentials and spikes in primary visual cortex convey independent visual information. *J. Neurosci.* **28** (22), 5696–5709 (2008).
39. Watts, D. J. & Strogatz, S. H. Collective dynamics of 'small-world' networks. *Nature* **393** (6684), 440–442 (1998).
40. Rulkov, N. F. Modeling of spiking-bursting neural behavior using two-dimensional map. *Phys. Rev. E.* **65** (4), 041922 (2002).
41. Ullner, E., Zaikin, A., Garcıa-Ojalvo, J., Bascones, R. & Kurths, J. Vibrational resonance and vibrational propagation in excitable systems. *Phys. Lett. A.* **312** (5–6), 348–354 (2003).

42. Hudetz, A. G., Vizuete, J. A. & Pillay, S. Differential effects of isoflurane on high-frequency and low-frequency γ oscillations in the cerebral cortex and hippocampus in freely moving rats. *Anesthesiology* **114** (3), 588 (2011).
43. Pitzschke, A. et al. Red and NIR light dosimetry in the human deep brain. *Phys. Med. Biol.* **60** (7), 2921–2937 (2015).
44. Zhang, Y., Zhao, Y., Li, W., Qian, Z. & Xing, L. Enhancement of microvessel in laser speckle image using Gaussian kernel template. *J. Innov. Opt. Health Sci.* (2019).
45. Eggermont, J. J. & Kenmochi, M. Salicylate and quinine selectively increase spontaneous firing rates in secondary auditory cortex. *Hear. Res.* **117** (1–2), 149–160 (1998).
46. Eisenkolb, V. M. et al. Human acute microelectrode array recordings with broad cortical access, single-unit resolution, and parallel behavioral monitoring. *Cell. Rep.* ;**42**(5) (2023).
47. Ilic, S. et al. Effects of power densities, continuous and pulse frequencies, and number of sessions of low-level laser therapy on intact rat brain. *Photomed. Laser Surg.* **24** (4), 458–466 (2006).
48. Yu, H. et al. Multiple stochastic resonances and Oscillation transitions in cortical networks with time delay. *IEEE Trans. Fuzzy Syst.* **28** (1), 39–46 (2018).


## Acknowledgements

This work was supported by National Natural Science Foundation of China (82202295, 82151311 and 82201652), Natural Science Foundation of Jiangsu Province (BK20210531), the Fundamental Research Funds for the Central Universities (NZ2024032, NP2024102, NJ2024016 and NJ2024029), the Jiangsu Funding Program for Excellent Postdoctoral Talent (2024ZB661), and the Key Project of Nanjing Health Science and Technology Development Special Fund (ZKX24043).

## Author contributions

P.Z., L.Y. wrote the manuscript. P.Z. prepared all figures. W.L., F.G. and Z.Q. supervised the project. L.Y. designed the study and contributed to the data collection. T.Y., X.J., Y.L, W.X. and W.J. assisted in revising the manuscript and provided critical comments.

## Declarations

## Competing interests

The authors declare no competing interests.

## Additional information

**Supplementary Information** The online version contains supplementary material available at https://doi.org/10.1038/s41598-025-21252-7.

**Correspondence** and requests for materials should be addressed to X.J., F.G. or Z.Q.